

3D image based stochastic micro-structure modelling of foams for simulating elasticity

Anne Jung and Claudia Redenbach and Katja Schladitz and Sarah Staub

Abstract Image acquisition techniques such as micro-computed tomography are nowadays widely available. Quantitative analysis of the resulting 3D image data enables geometric characterization of the micro-structure of materials. Stochastic geometry models can be fit to the observed micro-structures. By alteration of the model parameters, virtual micro-structures with modified geometry can be generated. Numerical simulation of elastic properties in realizations of these models yields deeper insight on the influence of particular micro-structural features. Ultimately, this allows for an optimization of the micro-structure geometry for particular applications. Here, we present this workflow at the example of open cell foams. Applicability is demonstrated using an aluminum alloy foam sample. The structure observed in a micro-computed tomography image is modelled by the edge system of a random Laguerre tessellation generated by a system of closely packed spheres. Elastic moduli are computed in the binarized μ CT image of the foam as well as in realizations of the model. They agree well with the results of a compression test on the real material.¹

Anne Jung
Universität des Saarlandes, Technical Mechanics, Saarbrücken, Germany, e-mail: anne.jung@mx.uni-saarland.de

Claudia Redenbach
Technische Universität Kaiserslautern, Mathematics Department, Kaiserslautern, Germany, e-mail: redenbach@mathematik.uni-kl.de

Katja Schladitz
Fraunhofer-Institut für Techno- und Wirtschaftsmathematik, Kaiserslautern, Germany, e-mail: katja.schladitz@itwm.fraunhofer.de

Sarah Staub
Fraunhofer-Institut für Techno- und Wirtschaftsmathematik, Kaiserslautern, Germany, e-mail: sarah.staub@itwm.fraunhofer.de

¹ This is a preprint of the following chapter: Anne Jung, Claudia Redenbach, Katja Schladitz, and Sarah Staub: 3D Image-Based Stochastic Micro-structure Modelling of Foams for Simulating Elasticity, published in Research in Mathematics of Materials Science. Associa-

1 Introduction

3D image data, predominantly generated by computed tomography, have been analyzed for more than 30 years now. In medical applications, the emphasis has been on segmentation and visualization. Algorithmic foundations had been settled in the 1990es, see [37] for a comprehensive overview.

Quantitative analysis of 3D images of micro-structures started in the 1990es, too, with porous rock samples [8, 59] and trabecular bone [18]. Prediction of macroscopic, in particular mechanical, properties based on the observed micro-structure has been a goal right from the beginning [64].

The seminal paper [29] provided Ohser's algorithm for efficiently estimating the intrinsic volume densities based on 3D binary images, linking fundamental characteristics of random closed sets [10, 15, 57] to those observable in image data.

Our contributions to predicting macroscopic materials properties by numerical simulation in realizations of 3D stochastic geometry models started with acoustic adsorption [52] and had been concerned with rigid foams early on [17, 48]. After establishing the mathematical [30] and algorithmic [31] bases for modelling cellular materials structures, elastic properties were studied [50]. Here, we will concentrate on characterization and modelling of rigid foams, too. Some typical examples of these materials are shown in Figure 1.

Stochastic modelling allows for detailed studies of structure property relations [12, 34, 65]. Geometric features closely tied in practice can be modified individually. The use of stochastic instead of deterministic geometry models naturally captures microscopic heterogeneity as well as macroscopic homo-

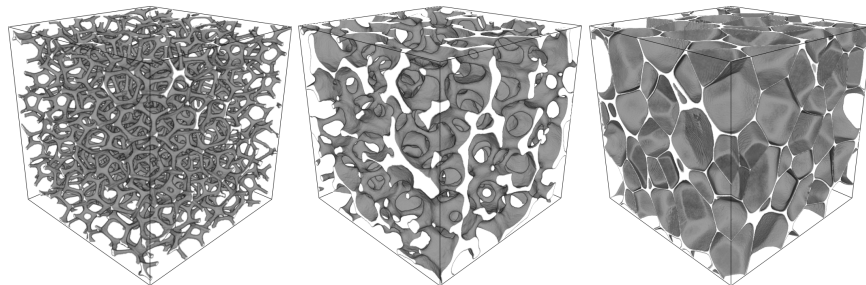


Fig. 1 Visualizations of 500^3 voxel sub-volumes from reconstructed CT images of rigid foams. From left to right: open polymer, partially closed ceramic, and closed polymer foams. All CT scans taken at ITWM with voxel sizes $49\ \mu\text{m}$ for the open polymer foam, $34\ \mu\text{m}$ for the ceramic foam, and $3\ \mu\text{m}$ for the closed polymer foam. Samples provided by Vesuvius (ceramic) and Evonik (closed polymer foam).

generality assuming invariances of the underlying distribution law. Moreover, the size of the representative volume element (RVE) can be determined statistically [19, 26]. In this work, we investigate RVE of constant size corresponding to the size of the foam samples characterized experimentally. Alternatively, more, but smaller volume elements in the sense of stochastic homogenization as devised e. g. in [3] could be used. In the case of rigid foams, the size of these volume elements is surely bounded by one foam cell. The theory of homogeneous random closed sets provides the corresponding mathematical concept by the typical cell of a tessellation [57]. Exploring this alternative approach and comparing the two are subject of future research. Fitting stochastic geometry models to the observed real structure is tedious as analytic relations are available only for models not suitable for real materials. Starting at the real micro-structure ensures however that observed trends and correlations have a practical meaning.

The concept of statistically similar representative volume elements (SS-RVE) [5] is similar to our approach in the sense of fitting the synthetic structure to the real one by minimizing the weighted sum of the squared differences of several geometric characteristics estimated for both, real and synthetic structure. It differs however fundamentally in aiming at deterministic, geometrically significantly simplified structures right from the beginning. Simple structures consisting e.g. of just a couple of spheres are used to generate the SSRVE that is subsequently periodically continued.

Here, we focus on numerical computation of effective elastic properties of an aluminum alloy foam by homogenization. The foam sample's micro-structure is observed in 3D image data obtained by micro-computed tomography (μ CT). We use both, the segmented image data as well as a random Laguerre tessellation model fit to the observed foam structure based on the estimated geometric characteristics. We provide the basics on random closed sets, their characteristics, in particular the densities of the intrinsic volumes, and estimating them based on 3D image data in Section 2. The image processing workflow for dividing the pore space of open foams into individual image objects is described in the same section. Section 3 is dedicated to random Laguerre tessellations and fitting them to the observed structure.

Simulation of elastic properties in voxel representations of the real foam or of model realizations is described in Section 4. A computational homogenization scheme [62] is used to transition from the microscopic scale of the foam structure to the macroscopic scale of the effective properties. A comprehensive overview on this class of homogenization schemes is given in [13]. A microscopic boundary value problem is formulated by imposing admissible boundary conditions and subsequently solved numerically, by a Finite Element Method [11] or a fast Fourier transform (FFT) based solution of the Lippmann-Schwinger (LS) equations of elasticity [42]. Efficiency in terms of computational effort and memory use is critical as the images consist of several hundreds of voxels in each direction. The LS-FFT homogenization applied here is described in Section 4.

Finally, in Section 5, we apply the methods from Sections 2-4 to the real aluminum foam sample. A random Laguerre tessellation is fit to the foam structure based on the characteristics estimated from the segmented CT image. Four synthetic foams are derived from its edge system by applying two cross-sectional shapes of the struts and relaxing the foam or not. Elastic properties derived by computation in the segmented μ CT image and the structural modulus measured experimentally are compared in 5.3. The effective stiffnesses of the synthetic foams are numerically predicted in 5.3.2.

2 3D image analysis for foams

We introduce the general concept of random closed sets, define basic characteristics for them, and describe how to estimate these characteristics based on 3D volume images as generated by computed tomography.

2.1 *Random closed sets and their characteristics*

Materials micro-structures are often macroscopically homogeneous in some sense but locally heterogeneous. A commonly used mathematical model for such structures are random closed sets, random variables whose realizations are closed subsets of \mathbb{R}^3 . Schneider and Weil [57] attribute the concept to Matheron [39] and Kendall [27], with the first detailed description being [40].

Denote by \mathcal{F} the system of closed subsets of \mathbb{R}^3 and by \mathfrak{F} the hit-or-miss σ -algebra generated by the sets $\{F \in \mathcal{F} : F \cap A \neq \emptyset\}$ for all compact $A \subset \mathbb{R}^3$. The pair $(\mathcal{F}, \mathfrak{F})$ is then a measurable space and we can define random closed sets (RACS) as random variables with values in this space. More precisely, let $(\Omega, \mathcal{A}, \mathbb{P})$ be a probability space. A random closed set Ξ is a measurable mapping

$$\Xi : (\Omega, \mathcal{A}, \mathbb{P}) \mapsto (\mathcal{F}, \mathfrak{F}).$$

We call Ξ stationary (or macroscopically homogeneous) and isotropic if its distribution is invariant with respect to translations and rotations, respectively.

Point processes

One class of RACS models are locally finite random closed sets: Denote by \mathcal{C} the system of compact subsets of \mathbb{R}^3 . A set $A \subseteq \mathbb{R}^3$ is locally finite if $\#(A \cap C) < \infty$ for any $C \in \mathcal{C}$. Here $\#B$ refers to the number of elements of the set B . A (simple) point process Φ is a random variable with values

in the system of locally finite sets and can be read as a sequence of random points in \mathbb{R}^3 as well as a random counting measure. The measure Λ defined by $\Lambda(B) = \mathbb{E}(\#\Phi \cap B)$ is called the intensity measure of Φ . For stationary point processes, it is a multiple of the Lebesgue measure $\Lambda(B) = \lambda V(B)$ with the intensity $\lambda > 0$ giving the mean number of points per unit volume.

The Poisson point process

The Poisson point process representing complete spatial randomness plays a particular role as it is analytically tractable and the basis for constructing other point process as well as a variety of random closed set models. A Poisson point process Φ in \mathbb{R}^3 with intensity measure Λ is a point process with the number of points $\#\Phi \cap B$ in a Borel set B being Poisson distributed with parameter $\Lambda(B)$ and the numbers of points $\#\Phi \cap B_1, \dots, \#\Phi \cap B_n$ in pairwise disjoint Borel sets B_1, \dots, B_n being independent random variables.

As a consequence, a stationary Poisson point process with intensity λ in a compact observation window $W \subset \mathbb{R}^3$ can easily be simulated by first drawing the number of points Poisson distributed with parameter $\lambda V(W)$. Then, the points are placed independently identically uniformly distributed in W . There is no interaction of the points. This is why the Poisson point process is used as reference for complete spatial randomness.

The random points can additionally be decorated by marks representing for instance a species, age, or size. Moreover, the definitions of point process and Poisson point process can directly be transferred any locally compact space with countable base.

2.1.1 Intrinsic volumes

The intrinsic volumes are basic characteristics of RACS. Let \mathcal{K} denote the system of compact and convex sets (convex bodies) in \mathbb{R}^3 . Dilating $K \in \mathcal{K}$ with a ball of radius r yields the so-called parallel set $K \oplus b(0, r) := \{x + y : x \in K, y \in b(0, r)\}$. Steiner's formula expresses the volume of this set as a polynomial in r :

$$V(K \oplus b(0, r)) = \sum_{k=0}^3 \kappa_k V_{3-k}(K) r^k, \quad r \geq 0,$$

where κ_k is the volume of the k -dimensional unit ball and the coefficients V_0, \dots, V_3 , are the four intrinsic volumes in \mathbb{R}^3 . These are – up to constant factors – the volume $V = V_3$, the surface area $S = 2V_2$, the integral of mean curvature $M = \pi V_1$, and the Euler number $\chi = V_0$, see e. g. [56, p. 210]. For $K \in \mathcal{K}$, the integral of mean curvature is up to a constant the mean width

$M = 2\pi\bar{b}$ – the distance of two parallel planes enclosing K , averaged w.r.t. rotation.

The intrinsic volumes form a basis of geometric characteristics in the sense of Hadwiger’s theorem [57, Theorem 14.4.6]: Every rigid motion invariant, additive, and continuous functional on \mathcal{K} is a linear combination of the intrinsic volumes. Additivity yields a straightforward extension of the intrinsic volumes to finite unions of convex bodies, so-called polyconvex sets.

2.1.2 Densities of the intrinsic volumes

The intrinsic volumes can be used to characterize single cells of a foam. For characterizing the complete solid component, we need another generalization. It applies for RACS Ξ whose intersections with convex, compact observation windows $W \in \mathcal{K}$ are almost surely polyconvex. In this case, the intrinsic volumes of $\Xi \cap W$ are well-defined, too. Denote by $\mathbb{E}V_k(\Xi \cap W)$ the expected k -volumes of this intersection with respect to the distribution of Ξ .

The *densities of the intrinsic volumes* are the limits of these expectations for growing observation window:

$$V_{V,k}(\Xi) = \lim_{r \rightarrow \infty} \frac{\mathbb{E}V_k(\Xi \cap rW)}{V(rW)}, \quad k = 0, \dots, 3. \quad (1)$$

The limit exists if $\mathbb{E}2^{N(\Xi \cap [0,1]^3)} < \infty$ [57, Theorem 9.2.1], where $N(X)$ is the smallest $m \in \mathbb{N}$ such that $X = K_1 \cup \dots \cup K_m$ with $K_1, \dots, K_m \in \mathcal{K}$.

Of particular interest for foams are the (solid) volume fraction $V_V = V_{V,3}$, with $p = 1 - V_V$ being the porosity, and the specific surface area $S_V = 2V_{V,2}$. Additionally, the density of the Euler characteristic $\chi_V = V_{V,0}$ is related to the mean number of nodes of the foam skeleton per unit volume [53].

2.2 Image analysis

We quickly define the basic concepts image and adjacency system, discuss the segmentation tasks posed by our problem, and finally describe how to estimate the characteristics needed for model fitting later on.

2.2.1 Images

A typical way of observing a realization X of a suitable RACS Ξ is via discretization in a 3D image. For simplicity, let \mathbb{Z}^3 be a three-dimensional cubic lattice with lattice spacing $s > 0$. Denote by $W \subset \mathbb{R}^3$ a cuboidal observation window. By an image we understand a function

$$f : \cap W \longrightarrow V,$$

where V is the set of real or complex numbers \mathbb{R} , \mathbb{C} , or $V = \{0, \dots, 2^n - 1\}$ with $n = 1, 8, 16$ or 32 .

Black-and-white images f with $V = \{0, 1\}$ are often called binary image. In this case, the image foreground can be identified with the intersection $X \cap \cap W$ of a set $X \subset \mathbb{R}^3$ observed at the lattice points in the observation window W . The function f is then the indicator function of X , restricted to the observable points $f = \mathbb{I}_X|_{\cap W}$. That is, $f(x) = 1$ if $x \in X \cap \cap W$ and $f(x) = 0$ otherwise. Usually, in image processing, both $x \in \cap W$ and the pair $(x, f(x))$ are called pixel (or voxel).

Mathematically, we interpret an image as a set of lattice points equipped with grayvalues, not as a set of small cubes. We nevertheless address the lattice spacing s as pixel or voxel size, too.

By construction, the pixels of a 3D image are discrete. To represent concepts such as the connected components of a RACS in an image, a notion of connectivity of pixels must be introduced. To define the discrete connectivity in 3D unambiguously, we follow [44] in using adjacency systems consisting of j -dimensional faces with $j = 0, \dots, 3$. The *discretization* $X \sqcap \mathbb{F}$ of a compact subset $X \subset \mathbb{R}^3$ w. r. t. a given adjacency system \mathbb{F} is defined as the union of the elements F of \mathbb{F} whose vertices $\mathcal{F}^0(F)$ are contained in X

$$X \sqcap \mathbb{F} = \bigcup \{F \in \mathbb{F} : \mathcal{F}^0(F) \subseteq X\}.$$

It can be interpreted as an approximation of X by a polyhedral set built using the bricks provided by the adjacency system. For background on adjacency systems and consistent connectivity for foreground and background of an image, see [43, 44, 45, 46, 51].

2.2.2 Segmentation

Segmentation subsumes a wide variety of methods assigning pixel values to classes, usually coded by integer values. Here, we have to solve two segmentation tasks: First, we have to binarize the image f to get hold of the solid foam structure. Second, we exploit moments of the distributions of cell characteristics in the model fitting step. Hence, we have to identify foam cells or pores as image objects. This second segmentation task is much more demanding, as the cells of an open foam are connected. As a consequence, the background or pore space has to be divided to "reconstruct" the cell structure.

Binarization

Very roughly, computed tomography generates 3D images with voxel gray-values related to the mean X-ray absorption of the small sub-volume they represent. Solid material structure thus appears brighter than air. For binarizing the image, we look for a transformation

$$T(f) : \cap W \longrightarrow \{0, 1\}$$

such that $T(f) \equiv 1$ corresponds to the solid foam material X observed in $\cap W$ as described above. The simplest way to achieve a binarization, is just to use a global grayvalue threshold $\theta \in \mathbb{R}$

$$T(f)(x) = \begin{cases} 1 & f(x) \geq \theta \\ 0 & \text{else} \end{cases} .$$

This simple binarization method can of course be applied only, if the image is free of global grayvalue fluctuations. Prior to binarization, we apply a median filter with a $3 \times 3 \times 3$ filter mask to reduce noise and smooth the foam's surface slightly. Subsequently, the global grayvalue threshold θ can be chosen by Otsu's method [47].

Cell reconstruction

Now we separate the multiply connected pore system of the foam into individual image objects by a combination of two strong morphological tools, the Euclidean distance transform and the watershed transform.

Let $X \subseteq \mathbb{R}^3$ be the set under consideration, here the pore space of the foam. The Euclidean distance transform maps each point in \mathbb{R}^3 to its shortest distance to the complementary set $\mathbb{R}^3 \setminus X$,

$$\text{EDT} : \mathbb{R}^3 \mapsto [0, \infty) : x \mapsto \min\{\|x - y\| : y \in \mathbb{R}^3 \setminus X\}.$$

This results in $\text{EDT}(y) = 0$ for all $y \in \mathbb{R}^3 \setminus X$ and local maxima in the centers of spherical regions in X . Inverting the EDT image $\text{EDT}(X \cap \cap W)$ turns these local maxima into minima: $f(x) = \max\{\text{EDT}(X \cap \cap W)\} - \text{EDT}(x)$. The exact Euclidean distance transforms can be calculated very efficiently, i.e. in linear time, exploiting the Voronoi paradigm [41].

Now the watershed transform assigns a connected region to each local minimum. This transform can be interpreted as the flooding of the topographic surface $\{(x, f(x)) : x \in \cap W\}$: water rises uniformly with growing grayvalue f from all local minima. Watersheds are formed by all pixels where water basins filled from different sources meet. Finally, the image is segmented into regions and the system of watersheds dividing them [66].

In practice, this morphological separation strategy suffers from superfluous local minima in the inverted EDT (iEDT) image due to discretization, imperfect binarization, and cell shapes deviating from spherical. The watershed transform assigns each such minimum a region, inevitably resulting in a strong over-segmentation. A remedy for this is to prevent small regions from arising at all by altering the flooding accordingly (pre-flooded watershed, [63]). The foam structure under consideration here is rather regular. Predescribing a minimal cell volume is thus easily applicable. See Figure 2 for an illustration using 2D sections through the 3D images.

It is remarkable that the heavyweights in this segmentation procedure – watershed transform and EDT – as devised by [66] and [41] work "as is" in arbitrary dimensions. Often, image processing methods are mathematically easily formulated for arbitrary dimensions and applied to 2D images. Practical application in higher dimensions is nevertheless often impossible due to computational complexity or ambiguities, e.g. arising from the existence of two subdimensions or connectivity issues.

2.2.3 Estimating the intrinsic volumes based on image data

The intrinsic volumes and their densities can be estimated based on 3D image data very efficiently by Ohser's algorithm [29]. This algorithm codes the $2 \times 2 \times 2$ voxel configurations in a binary image using a convolution with a cubic filter mask assigning weights 2^k , $k = 0, \dots, 7$ to the vertices of the cube. The gray value histogram of the resulting 8bit gray value image contains all information needed to derive the intrinsic volumes by multiplication with a suitable weights vector. See [46] for details.

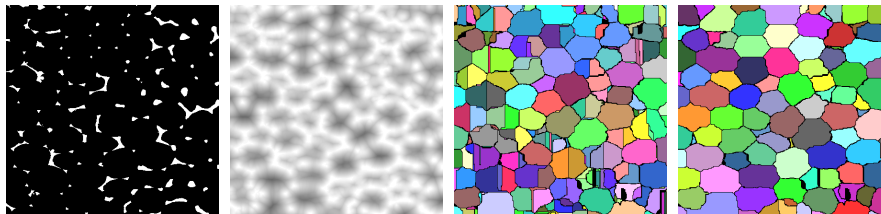


Fig. 2 Morphological cell reconstruction, illustrated using 2D slices of the 3D image. Left: Binarized - solid foam structure appearing white, pore space black. Center, left: Inverted Euclidean distance map on the pore space, small values dark, high white. Center, right: Pore system generated by the watershed transform. Right: Pore system generated by the pre-flooded watershed transform.

3 Random Laguerre tessellations and fitting them

Laguerre tessellations are a generalization of the well-known Voronoi tessellation model. When generated by random sphere packings, they reflect the topology of rigid foams very well and enable particularly good control over the volume distribution of the resulting cells. We recall the concept and a fitting strategy.

3.1 Laguerre tessellations generated by random sphere packings

Let T be a set of bounded convex three-dimensional subsets of \mathbb{R}^3 , the cells of T . The system T is called a tessellation of \mathbb{R}^3 if T is space-filling, i.e. $\bigcup_{C \in T} C = \mathbb{R}^3$, and if the interiors of different cells do not intersect. Convexity of the cells and T being space-filling force the cells to be three-dimensional polytopes (3-polytopes) [57, Lemma 10.1.1].

Write

$$F(x) = \bigcap_{C \in T, x \in C} C, \quad x \in \mathbb{R}^3$$

for the intersection of all cells of T containing the point x . Then $F(x)$ is a non-empty finite intersection of 3-polytopes and hence a k -polytope, $k \in \{0, \dots, 3\}$. The set

$$\Delta^k(T) := \{F(x) : \dim F(x) = k, \quad x \in \mathbb{R}^3\}, \quad k = 0, \dots, 3,$$

is the set of k -faces of the tessellation T . We denote by $\mathcal{F}^k(C)$ the set of all k -faces, $k = 0, \dots, 3$, of a 3-polytope C . For a set \mathbb{F} of convex polytopes write $\mathcal{F}^k(\mathbb{F}) = \bigcup \{\mathcal{F}^k(F) : F \in \mathbb{F}\}$.

The tessellation T is called face-to-face if the faces of the tessellation coincide with the faces of the cells. If additionally exactly four cells meet in a vertex and three cells meet in an edge, the tessellation is called normal. A random tessellation is face-to-face or normal if its realizations almost surely have these properties.

Due to Plateau's laws, soap froths are normal, too [67]. Normal tessellations are thus a natural choice for modelling foam structures. The best known and most used tessellation model is the Voronoi tessellation that can be defined in arbitrary dimension n based on a locally finite set $\varphi \subset \mathbb{R}^n$ of generators. The Voronoi tessellation of φ consists of the cells

$$C(x) := \{z \in \mathbb{R}^n : \|x - z\| \leq \|y - z\|, \text{ for all } y \in \varphi\}, \quad x \in \varphi.$$

The size of a Voronoi cell thus only depends on the distance of its generator to the neighboring generators.

To gain more flexibility regarding cell shapes and in particular sizes, we use Laguerre tessellations. In this weighted generalization of the Voronoi tessellation, each generating point $x \in \mathbb{R}^n$ is assigned a positive weight $r > 0$ that can be interpreted as radius of a sphere with center x . The Laguerre cell of $(x, r) \in \varphi$ is defined as

$$C((x, r), \varphi) := \{z \in \mathbb{R}^3 : \|x - z\|^2 - r^2 \leq \|y - z\|^2 - s^2, \text{ for all } (y, s) \in \varphi\}.$$

The Laguerre tessellation $L(\varphi)$ is the set of the non-empty Laguerre cells of φ . The Voronoi tessellation corresponds to the special case of the Laguerre tessellation generated by a system of spheres of constant radius.

Laguerre tessellations are the most general model satisfying our assumptions: Each normal tessellation of \mathbb{R}^3 with convex cells is a Laguerre tessellation [4, 32].

In Laguerre tessellations, empty cells as well as cells not containing their generators can occur. Laguerre tessellations generated by non-overlapping spheres are however free of such irregularities, see Figure 3 for examples in \mathbb{R}^2 .

Random systems of closely packed spheres like those generated by the force-biased algorithm [7, 6] are well suited to generate Laguerre tessellations with prescribed cell volume distribution [49]. The cell shape is however rather restricted. In particular, the edge length distributions in Laguerre tessellations generated by dense packings of spheres are known to differ significantly from those observed in real foams, see [65]. This problem can be alleviated by relaxing the structure using the Surface Evolver [9].

Voronoi or Laguerre tessellations generated by stationary and isotropic (marked) point processes are also isotropic. In contrast, real foam structures often show anisotropies as their cells are elongated in particular directions due to the foam generation process. A simple way of incorporating this anisotropy into the models is by appropriate scaling of the cell systems.

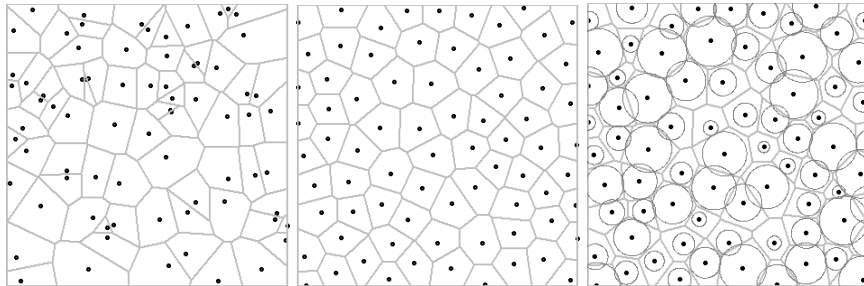


Fig. 3 Left and middle: Realizations of Voronoi tessellations generated by a Poisson point process and a regular point process. Right: Laguerre tessellation generated by the same point pattern as in the middle.

3.2 *Fitting a tessellation model*

Two strategies of fitting Laguerre tessellation models can be found in the literature. Laguerre approximation aims at finding a Laguerre tessellation that represents the observed cell system best in the sense that discrepancy between the observed cells and the cells of the approximation is minimized [33, 60]. Alternatively, a parametric tessellation model can be fit. That is, the observed cell system is approximated in a stochastic sense. The model is supposed to fit distributions of cell characteristics such as the volume, surface area or number of facets [31, 49]. The former approach yields an exact representation of the observed structure in the class of Laguerre tessellations. Here, we concentrate on the latter approach, as it allows for generating an arbitrary number of model realizations of basically arbitrary size.

The deviation of the model realization from the real observed foam structure is measured using the relative distance measure

$$\rho(\hat{m}, m) = \sqrt{\sum_{i=1}^n \left(\frac{m_i - \hat{m}_i}{\hat{m}_i} \right)^2}, \quad (2)$$

where $\hat{m} = (\hat{m}_1, \dots, \hat{m}_n)$ and $m = (m_1, \dots, m_n)$ are moments of the distributions of geometric characteristics of the cells of the original foam and the model, respectively. For rigid foams whose structure is observed in 3D images, the means and standard deviations of the volume $V = V_3$, the surface area $S = 2V_2$, the mean width $\bar{b} = \frac{1}{2}V_1$, and the number of facets F_C of the cells have proven to be particularly well suited [31, 49]. The choice is based on mean value relations for normal random tessellations, see [10, Section 9.4].

For minimizing the distance measure (2) on the parameter space of a tessellation model, one would ideally use analytic formulas relating the model parameters and the required moments of cell characteristics. Unfortunately, only Laguerre tessellations generated by a homogeneous Poisson process are analytically tractable [32]. For Laguerre tessellations generated by random sphere packings, model fitting therefore has to rely on Monte Carlo simulations of model realizations.

The cell volumes in cellular materials are usually assumed to be lognormal or gamma distributed. Moreover, Laguerre tessellations of dense packings of spheres with lognormal and gamma distributed volumes are very regular and therefore well suited to model rigid foams. In [49], model realizations for various packing fractions κ and coefficients of variation c of the volume distribution were generated. Subsequently, polynomials in c were fitted to the estimated geometric characteristics for each value of κ . Using these results, the minimization of $\rho(\hat{m}, m)$ in (2) reduces to minimizing a polynomial thus allowing for quick and easy model fit.

4 Numerical simulation of elastic properties

The following subsections outline the simulation of the effective mechanical stiffness of inhomogeneous micro-structures such as foams. Therefore, the averaged stresses and strains are defined as volume averages over their microscopic counterparts. Furthermore, the fundamentals of the solution of the microscopic boundary value problem in terms of an LS-FFT are outlined briefly.

4.1 *Effective properties of micro-structured materials*

We apply a computational homogenization scheme to determine the effective stiffness of the foam numerically. In this scheme, the microscopic geometry of the structure is captured either by a CT image of the foam or a realization of a stochastic geometry model. Furthermore, the mechanical properties of the micro-constituents, here the Young's modulus and Poisson's ratio, are required.

The micro-structure is captured in volume element $\Omega \subseteq \mathbb{R}^3$ with volume $V(\Omega)$ and boundary $\partial\Omega$. The effective stiffness of this structure \mathbb{C}^* connects the averaged stresses $\langle\sigma\rangle$ and strains $\langle\varepsilon\rangle$ via

$$\langle\sigma\rangle = \mathbb{C}^* : \langle\varepsilon\rangle. \quad (3)$$

The $:$ in equation (3) denotes the double inner product between the fourth order tensor \mathbb{C}^* and the second order tensor $\langle\varepsilon\rangle$ and corresponds to the mapping of the strains to the stresses (compare Hooke's law in one-dimensional elasticity $\sigma = E\varepsilon$). The averaged stresses and strains are defined as volume averages of their microscopic counterparts as

$$\langle\sigma\rangle := \frac{1}{V(\Omega)} \int_{\Omega} \sigma(x) dx \quad \text{and} \quad \langle\varepsilon\rangle := \frac{1}{V(\Omega)} \int_{\Omega} \varepsilon(x) dx. \quad (4)$$

For the numerical computation of the effective foam properties, a displacement, which corresponds to a constant strain in a homogeneous reference material, is applied to the boundary of the volume element. Due to the possible anisotropy of the foam, six loadcases are computed – three tension, three shear as sketched in Figure 4.

After solving the six microscopic boundary value problems, we compute the complete effective stiffness tensor \mathbb{C}^* .

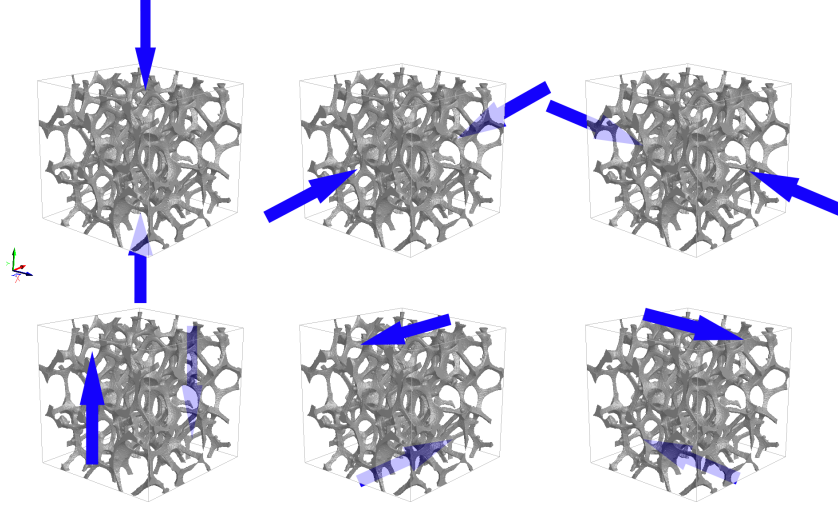


Fig. 4 Application of boundary conditions for homogenization. Blue arrows indicate the forces applied.

4.2 Lippmann-Schwinger Fast Fourier Transform based solver

In the following, details on the solution of the boundary value problem are outlined. Our microscopic simulation is based on the solution of the Lippmann-Schwinger (LS) equations for elasticity, see [36] and [68]. The required Green's operator is explicitly known in the Fourier space. Thus, these equations are solved efficiently by application of a fast Fourier transform (FFT). This LS-FFT scheme is implemented in ITWM's micro-structure solver FeelMath, see [22] and [24], also available as module ElastoDict [1] in the commercial software GeoDict [2]. The LS-FFT solver enables precise computation of microscopic stresses and strains directly in μ CT images or other voxel based three-dimensional structures. It is applicable to porous structures and therefore suitable for the open aluminum foam considered here.

In the solver, the equilibrium equation of the Cauchy stress σ

$$\operatorname{div} \sigma(x) = 0, \quad x \in \Omega \quad (5)$$

is considered in the micro-domain Ω . The kinematics for the strains ε depending on the displacements u and the fluctuations v read

$$\left. \begin{aligned} \varepsilon(u)(x) &= \langle \varepsilon \rangle + \varepsilon(v)(x) \\ \varepsilon(v)(x) &= \frac{1}{2} (\operatorname{grad} v(x) + \operatorname{grad}^t v(x)) \end{aligned} \right\} \quad x \in \Omega \quad (6)$$

in terms of the applied macroscopic strain ε . At the boundary of the micro-structure $\partial\Omega$ (anti-)periodic boundary conditions are applied via

$$\left. \begin{array}{l} v(x) \\ \sigma(x) \cdot n(x) \end{array} \right\} \begin{array}{l} \# \\ -\# \end{array} \quad x \in \partial\Omega. \quad (7)$$

The symbol $\#$ refers to periodicity, i.e. the fluctuations at opposite faces of the boundary are equal, whereas $-\#$ denotes antiperiodicity, i.e. the tractions $\sigma \cdot n$ at opposite faces point into opposite directions, but have the same magnitude. The set of underlying equations is completed by a constitutive equation for the microscopic constituents. For the aluminum we restrict ourselves to the linear elastic case. Thus the microscopic stresses and strains are connected by an elasticity tensor \mathbb{C} via

$$\sigma(x) = \mathbb{C}(x) : \varepsilon(x) \quad (8)$$

which only depends on Young's modulus E and Poisson's ratio ν of the aluminum alloy. In the pores, the stiffness is set to zero. In general the presented approach is however suitable to capture more complex material behavior like inelasticity and rate-dependency, see [23, 54, 61].

Next, we focus on reformulating the periodic boundary value problem into an integral expression of the Lippmann-Schwinger type. To this end, we introduce a constant homogeneous reference stiffness tensor \mathbb{C}^0 instead of the stiffnesses of the aluminum and the pores. This homogeneous stiffness tensor is applied to define the polarization tensor τ as

$$\tau(x) = \sigma(x) - \mathbb{C}^0 : \varepsilon(x). \quad (9)$$

With the help of Green's operator Γ^0 associated with the reference stiffness, the solution of the equilibrium equation (3) reads

$$\varepsilon(x) = \langle \varepsilon \rangle - (\Gamma^0 * \tau)(x). \quad (10)$$

The convolution operator $*$ is defined by

$$(\Gamma^0 * \tau)(x) = \int_{\Omega} \Gamma^0(x-y) : \tau(y) \, dy. \quad (11)$$

Combining the constitutive law (6), the definition of the polarization stress (9), and the solution (10) yields the LS equation as

$$\varepsilon = \varepsilon(x) + \Gamma^0(x) * ((\mathbb{C}(x) - \mathbb{C}^0) : \varepsilon(x)) = (I + B_\varepsilon(x)) \varepsilon(x). \quad (12)$$

Green's operator Γ^0 does not depend on the fluctuations and thus only depends on the homogeneous reference stiffness \mathbb{C}^0 , see [28].

The LS equation (12) can be solved iteratively using the Neumann series expansion or by using the conjugate gradient method. As Green's operator is

explicitly known in Fourier space, the Fourier transform is applied. A more detailed description of the algorithm can be found in [61].

Note that the discretization by Fourier polynomials as presented in [42] leads to convergence problems for porous structures due to the infinite stiffness contrast of the microscopic constituents. Therefore we use a finite difference discretization based on a staggered grid, which converges also for highly porous materials, see [55]. A comprehensive overview of FFT-based homogenization methods is given in [54].

5 Application example

Now, all methods described above are applied to a real world open aluminum foam sample.

5.1 Material

We consider one of the open-cell aluminium alloy foam samples investigated in [20]. The sample made by CellTec Materials GmbH, Dresden, Germany consists of $\text{AlSi}_7\text{Mg}_{0.3}$, has nominal pore size 10 ppi (pores per inch) and mean density 0.156 g/cm^3 corresponding to a porosity of 94.2 %.

A cubic sample of edge length 40 mm is spatially imaged by μCT at voxel size $29.44 \mu\text{m}$. See Figure 5 for a volume rendering.

Larger samples of size $40 \text{ mm} \times 40 \text{ mm} \times 80 \text{ mm}$ were tested mechanically. Uniaxial compression and tensile tests were performed, where the samples had to be infiltrated by a resin to allow for clamping for the tensile tests. Details are described in [21]. In [20], the foam structure was image analyti-

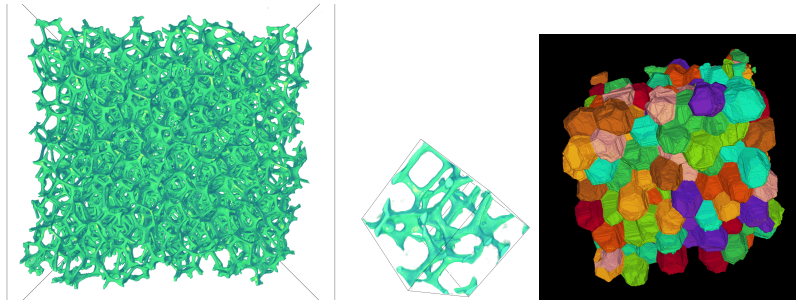


Fig. 5 Left: Volume rendering of the reconstructed CT image. The CT image taken at ITWM has originally a voxel size of $29.9 \mu\text{m}$ and the sample is contained in a cube of edge length 1 500 voxels corresponding to 4.5 cm. Center: sub-volume of edge length 0.9 cm with blob like production leftover. Right: System of reconstructed cells.

cally separated into vertices and struts. Mechanical behaviour of struts was investigated for five classes divided according to orientation.

5.2 Image analysis and model fit

The CT image of the foam was binarized by a global grayvalue threshold chosen according to Otsu’s method. Subsequently, the cells were reconstructed by the watershed on iEDT approach described in Section 2.2.2. Due to contamination of the foam structure (see Figure 5, middle), some cells were erroneously split into two parts. These errors were corrected manually.

Estimation of the mean cell diameters in the three coordinate directions reveals that cells are elongated by a factor $s = 1.2526$ in y -direction. The model fitting procedure detailed in Section 3.2 is formulated for isotropic structures. Hence, the structure is scaled by $1/s$ prior to the fitting. The cell characteristics estimated from the isotropic structure are listed in Table 1. Cells intersecting the boundary of the image are not observed completely. Hence, they are not included in the statistics. As larger cells are more likely to intersect the image boundary, ignoring boundary cells will result in a sampling bias. This is corrected by weighting the cells according to the inverse of their probability of being observed (Miles-Lantuejoul correction, [58, pp. 246]). In total, 336 cells with a total volume of $26\,246.11\text{mm}^3$ were included in the statistics.

The model fitting procedure returns a packing fraction of $\kappa = 60\%$ and a coefficient of variation $c = 0.414$ as optimal parameters when assuming a lognormal distribution of sphere volumes. Using these parameters, realizations of the tessellation models containing 820 cells are simulated in the unit cube. After rescaling the y -axis by the factor s , the tessellation edges are discretized into volume images. The voxel spacing for the discretization is chosen identical to the CT image, i.e. $29.44\,\mu\text{m}$. The images are cropped to a size of $1\,359^3$ voxels to obtain the original sample edge length of 40 mm.

Dilation of the edge system of the tessellations finally yields synthetic foam structures. Strut thickness is chosen such that the volume fraction is close to the value $V_V = 5.755\%$ estimated from the binarized CT image of the real foam. We consider two cross-sectional shapes of the struts – the simplest case of perfectly circular strut cross sections of constant radius and concave triangular struts. Additionally, to investigate the effect of relaxation, the tessellations are relaxed by using the Surface Evolver and also discretized with the two choices of strut cross sectional shape. That way, each realization of the Laguerre tessellation model yields four synthetic foam structures. All four synthetic foams are visualized in Figure 6.

Table 1 Estimated mean values and standard deviations of the cell characteristics of the aluminium foam and the best fit models for lognormally distributed volumes of the generating spheres.

| | | scaled data | | isotropic model | | | |
|-------|--------------------|-------------|--------|-----------------|-----------|--------|-----------|
| | | mean | std | mean | deviation | std | deviation |
| v | [mm ³] | 79.738 | 21.972 | 79.739 | ±0.00% | 26.598 | ±21.06% |
| s | [mm ²] | 104.468 | 22.241 | 98.608 | -5.61% | 19.832 | -10.83% |
| d | [mm] | 5.811 | 0.740 | 5.806 | -0.08% | 0.568 | -23.22% |
| F_C | | 13.828 | 2.256 | 14.06 | +1.69% | 2.173 | -3.71% |

5.3 Prediction of mechanical properties

We now predict the mechanical properties of the aluminum foam based on the binarized CT image and on realizations of the four synthetic foams.

5.3.1 Validation of simulation

Before actually predicting, we validate the numerical computation of the effective quantities with ElastoDict [1] by comparing with experimental data. To this end, a compression load case with a prescribed strain is simulated directly on the binarized CT image of the foam. The resulting effective stresses and the corresponding stiffness in the loading direction are calculated and compared to those determined by a compression test on the foam as described in [21].

First, we summarize the solver settings: The considered foam structure is not periodic. Hence, symmetric boundary conditions with free deformations in tangential directions are chosen. These symmetric boundary conditions and their compatibility with the periodic boundary conditions from Section 4.2 are described in detail in [14]. Thanks to the compatibility, this type of bound-

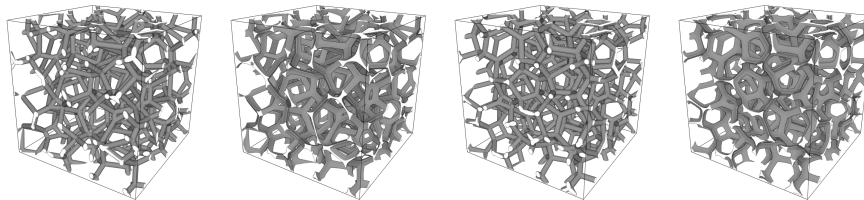


Fig. 6 Volume renderings of four synthetic foams derived from the same Laguerre tessellation model realization. From left to right: circular and triangular strut cross sections and their relaxed versions. Sub-volumes of 600³ voxels.

any condition is often referred to as periodicity compatible mixed uniform boundary conditions (PCMUBC). Generating a periodic structure by means of mirroring and effective implementation of PCMUBC in the context of FFT are connected in [14], too.

We apply composite voxels to reduce computation time as suggested in [25]. In this approach, the image is downsampled and the stiffness of the resulting mixed voxels or composite voxels is determined with the appropriate material of the rotated laminate, i.e. not only the local volume fraction is taken into account. Additionally, this mixing rule incorporates directional information on the material interface. Applying this strategy, we cut $1\,314 \times 1\,335 \times 1\,285$ voxels down to $328 \times 333 \times 321$ voxels, and consequently reduce CPU time and memory consumption significantly while keeping the loss of accuracy acceptable.

Second, we care for the material parameters: We restrict ourselves to the linear elastic case here. Therefore only Young’s modulus E_{Al} and Poisson’s ratio ν_{Al} of the aluminum at the micro-scale are required. Poisson’s ratio is taken from literature as $\nu_{Al} = 0.33$. Young’s modulus of the aluminum is chosen based on the experimental data from [16] measured in five different pores. The values are summarized in Table 2. In the simulations, the average

Table 2 Experimentally identified Young’s moduli for the aluminum alloy [16].

| Pore no. | Young’s modulus [MPa] |
|----------|-----------------------|
| 1 | 4 112 |
| 2 | 3 832 |
| 3 | 3 768 |
| 4 | 4 152 |
| 5 | 3 978 |

of these moduli (4 000 MPa) and the minimal and maximal values are considered. Attention should be paid to the fact that these values differ significantly from those usually reported for aluminum alloys ($\approx 70 \cdot 10^3$ MPa). These deviations are due to micro-porosity of the struts and inclusions resulting from the manufacturing process [38].

Figure 7 displays the experimental stress-strain curves of the five foam samples under compression in the linear loading regime, see [21] for the complete loading and unloading curves, and the effective stress-strain curves simulated directly in the complete binarized CT image. Simulated and experimental data match very well. Young’s modulus of the aluminum alloy is chosen as the average of the five samples summarized in Table 2.

Figure 8 shows how the microscopic Young’s modulus of the aluminum alloy influences the simulation result in terms of the effective modulus, i.e. the slope of the effective stress-strain curve. As input for the simulation, the

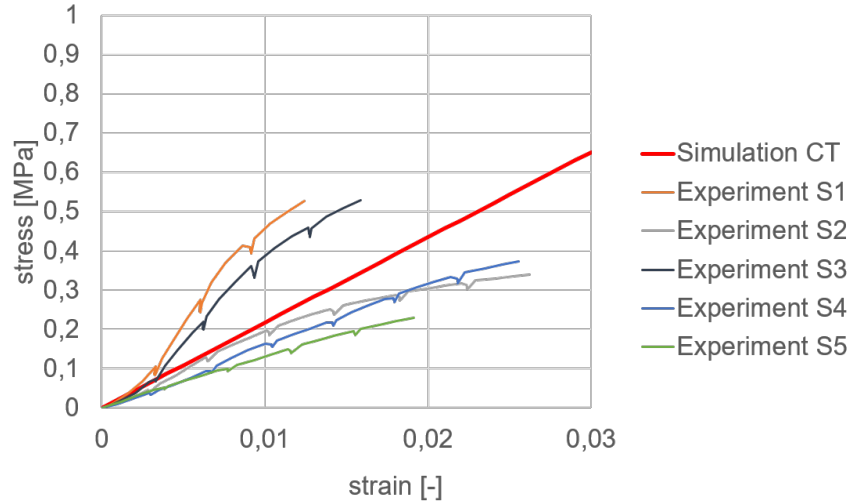
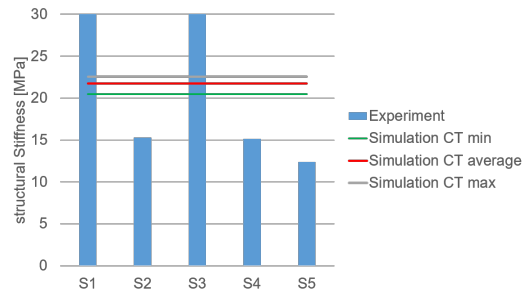


Fig. 7 Comparison of simulation and experiment in longitudinal direction y in terms of stress-strain diagram, Young's modulus of the aluminum $E_{Al} = 4000$ MPa.

minimal, maximal, and average values from Table 2 are considered. These simulation results are compared to the structural stiffness obtained by the compression experiments.

The structural stiffness corresponds to the slope of the experimental stress-strain curves in Figure 7. Clearly, variations of the microscopic Young's modulus in the considered range have only minor influence on the effective modulus. Therefore, we take only the average value of 4000 MPa into account in the following.

Fig. 8 Comparison of simulation and experiment in longitudinal direction y in terms of structural stiffness for varying Young's moduli of the aluminum alloy.



Validation of the simulation is completed by a comparison of the effective stresses simulated in the transversal directions (here x and z) and a compression experiment in the corresponding directions in Figure 9. The simulated effective stresses in x - and z -directions are almost the same and they are

much smaller than those in y -direction. Thus, the foam is much stiffer in the longitudinal y -direction. Figure 9 also shows that simulation and experiment also fit very well in the transversal directions.

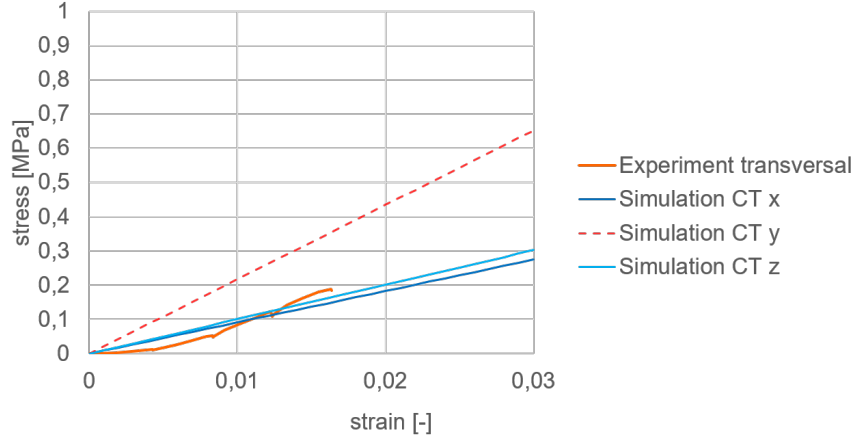


Fig. 9 Comparison of simulation and experiment in transversal direction, Young's modulus of the aluminum $E_{Al} = 4000$ MPa.

In the next section the validated simulation is applied to the synthetic foams derived from realizations of the Laguerre tessellation model fit in Section 5.2.

5.3.2 Effective mechanical properties of the synthetic foams

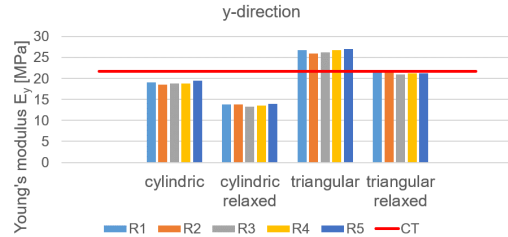
In order to predict the properties of the synthetic foams, five realizations of the Laguerre tessellation model yielding altogether 20 synthetic foams with circular or concave triangular struts, in relaxed state or not, are considered. All load cases displayed in Figure 4 are applied to each synthetic foam and the full effective stiffness tensor is computed. The effective Young's modulus in each direction (E_x , E_y and E_z) is approximated orthotropically, i.e. it is assumed that the inverse effective stiffness tensor reads

$$\mathbb{C}^{-1} = \begin{pmatrix} \frac{1}{E_x} & -\frac{\nu_{yx}}{E_y} & -\frac{\nu_{zx}}{E_z} & 0 & 0 & 0 \\ -\frac{\nu_{xy}}{E_x} & \frac{1}{E_y} & -\frac{\nu_{zy}}{E_z} & 0 & 0 & 0 \\ -\frac{\nu_{xz}}{E_x} & -\frac{\nu_{yz}}{E_y} & \frac{1}{E_z} & 0 & 0 & 0 \\ 0 & 0 & 0 & \frac{1}{G_{yz}} & 0 & 0 \\ 0 & 0 & 0 & 0 & \frac{1}{G_{zx}} & 0 \\ 0 & 0 & 0 & 0 & 0 & \frac{1}{G_{xy}} \end{pmatrix}, \quad (13)$$

where $\nu_{xy}, \nu_{xz}, \dots$ denote Poisson's ratios and G_{xy}, G_{zx}, G_{xy} the shear moduli in the corresponding directions.

We compare our simulation results to those obtained by direct simulations in the CT image. For the longitudinal (y) direction, the variations within one synthetic foam type do not influence the effective stiffness significantly, see Figure 10. For the two synthetic foam models with circular struts, the stiffness is underestimated. On the other hand, concave triangular struts lead to overestimation of the stiffness. The true strut cross section observed in the CT image of the real foam is in between both models - it is clearly triangular, but less concave than the model. The relaxed version of the synthetic foam with triangular struts is nevertheless able to reproduce the stiffness behavior in longitudinal direction of the real foam very well as the relaxation procedure reduces the effective stiffness for both strut geometries.

Fig. 10 Comparison of effective stiffness of synthetic and real foams in longitudinal direction. CT is the real foam's micro-structure as given by the binarized CT image. R1 to R5 are the five realizations of the fitted Laguerre tessellation model.



Analysis of the mechanical properties of the synthetic foams is completed by the stiffness in the transversal directions (x and z) reported in Figure 11. The anisotropic behavior of the real foam is captured by all synthetic foam models. The stiffness in the transversal directions is smaller than in longitudinal direction, agreeing with the experimental results as well as with those obtained by direct simulation in the binarized CT image. Not surprisingly, the two relaxed synthetic foams behave less anisotropic than their unrelaxed counterparts. Relaxation increases the effective stiffness in transversal direction, while it decreases the effective stiffness in longitudinal direction. The unrelaxed synthetic foam with the circular struts matches the mechanical behavior of the foam in transversal direction best.

In summary, all four synthetic foam models reproduce the mechanical compression behavior of the real aluminum foam well, including the anisotropy. Taking into account all three directions, the effective stiffness of the real foam is best reproduced by the unrelaxed synthetic foam with circular strut cross-sections, although the stiffness in longitudinal direction is slightly underestimated.

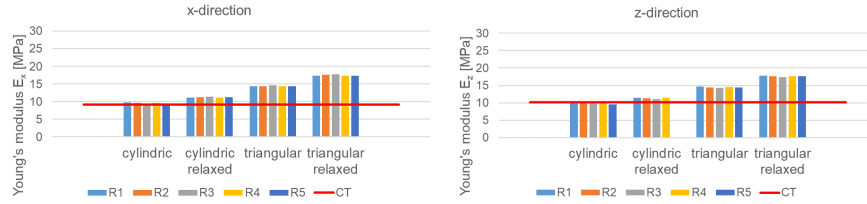


Fig. 11 Comparison of effective stiffness of synthetic (derived from R1 to R5) and real (CT) foams in transversal directions.

6 Conclusion

In this contribution, we describe completely the well-established, nevertheless rarely fully expanded workflow for simulating mechanical properties of a material based on stochastic geometry models of its micro-structure. Our use case is an open metal foam. Consequently, a random tessellation model is fit to it.

Stochastic geometry models not only capture naturally the microscopic heterogeneity of materials structures. Fitting them to the observed structure allows to generate many realizations as large as needed. Moreover, the effects of selected micro-structural geometric features can be investigated independently as demonstrated here for cross-sectional shape of the struts and relaxation. Model fitting and careful validation of the simulations further open the opportunity to determine the size of the representative volume and to devise optimized micro-structures.

Validation or calibration of the simulations by experiments is indispensable as the respective properties of the bulk material needed as input are hard to get. The values for the material e. g. in the struts can differ significantly from tabular values due to effects of the production process on scales finer than the micro-structure.

The elastic properties of the aluminum foam could be reproduced well by all four synthetic foams considered here. More sophisticated geometries might be needed when moving on to plastic properties. For instance, the local thickness of the struts could be fit [20, 35]. Moreover, real cellular structures can feature much more complex anisotropies due to production processes being based on polymer foams. In the latter, the foaming direction usually stands out. The structure might however be additionally distorted e. g. by the movement of a conveyor belt during foaming. Adequate characterization methods and modelling are subject of current research.

Acknowledgements We thank Franz Schreiber for the CT scans, Felix Arnold for assisting in the image processing of the CT image, and Sonja Föhst for providing the code for model simulation.

References

1. Elastodict. <https://www.geodict.de/Modules/Dicts/ElastoDict.php>
2. Geodict. <https://www.geodict.de/>
3. Armstrong, S., Kuusi, T., Mourrat, J.C.: Quantitative stochastic homogenization and large-scale regularity (2019)
4. Aurenhammer, F.: A Criterion for the Affine Equivalence of Cell Complexes in \mathbb{R}^d and Convex Polyhedra in \mathbb{R}^{d+1} . *Discrete & Computational Geometry* **2**, 49–64 (1987)
5. Balzani, D., Scheunemann, L., Brands, D., Schröder, J.: Construction of two- and three-dimensional statistically similar RVEs for coupled micro-macro simulations. *Comput. Mech.* **54**(5), 1269–1284 (2014). DOI 10.1007/s00466-014-1057-6
6. Bezrukov, A., Bargiel, M., Stoyan, D.: Statistical analysis of simulated random packings of spheres. Part. Part. Systems Char. **19**, 111–118 (2002)
7. Bezrukov, A., Stoyan, D., Bargiel, M.: Spatial statistics for simulated packings of spheres. *Image Anal. Stereol.* **20**, 203–206 (2001)
8. Biswal, B., Manwart, C., Hilfer, R.: Three-dimensional local porosity analysis of porous media. *Physica A: Statistical Mechanics and its Applications* **255**(3), 221–241 (1998). DOI [https://doi.org/10.1016/S0378-4371\(98\)00111-3](https://doi.org/10.1016/S0378-4371(98)00111-3). URL <https://www.sciencedirect.com/science/article/pii/S0378437198001113>
9. Brakke, K.A.: The surface evolver. *Experimental Mathematics* **1**(2), 141–165 (1992)
10. Chiu, S., Stoyan, D., Kendall, W.S., Mecke, J.: *Stochastic Geometry and Its Applications*, 3rd edn. Wiley, Chichester (2013)
11. Feyel, F., Chaboche, J.L.: Fe2 multiscale approach for modelling the elastoviscoplastic behaviour of long fibre sic/ti composite materials. *Computer Methods in Applied Mechanics and Engineering* **183**, 309–330 (2000)
12. Föhst, S., Osterroth, S., Arnold, F., Redenbach, C.: Influence of geometry modifications on the permeability of open-cell foams. *AIChE Journal* **68**(2), e17446 (2021) DOI 10.1002/aic.17446
13. Geers, M., Kouznetsova, V., Brekelmans, W.: Multi-scale computational homogenization: Trends and challenges. *J. Comput. Appl. Math.* **234**, 2175–2182 (2010)
14. Grimm-Strele, H., Kabel, M.: Fast Fourier transform based homogenization with mixed uniform boundary conditions. *Int. J. Num. Meth. Eng.* **122**(23), 7241–7265 (2021) DOI doi:10.1002/nme.6830
15. Hadwiger, H.: *Vorlesungen über Inhalt, Oberfläche und Isoperimetrie*. Springer-Verlag, Berlin (1957)
16. Heinze, S., Bleistein, T., Düster, A., Diebels, S., Jung, A.: Experimental and numerical investigation of single pores for identification of effective metal foams properties. *Zeitschrift für angewandte Mathematik* **98**, 682–695 (2018)
17. Helfen, L., Stanzick, H., Ohser, J., Schladitz, K., Rejmánková-Pernot, P., Banhart, J., Baumbach, T.: Investigation of the foaming process of metals by synchrotron-radiation imaging. In: B.M. Norbert Meyendorf George Y. Baaklini (ed.) *Proceedings SPIE 5045: Testing, Reliability, and Application of Micro- and Nano-Material Systems*, vol. 5045, pp. 254–265 (2003)
18. Hildebrand, T., Rüegsegger, P.: A new method for the model independent assessment of thickness in three-dimensional images. *Journal of Microscopy* **185**, 67–75 (1997)
19. Jeulin, D.: *Morphological Models of Random Structures*. Springer International Publishing, Cham (2021). DOI 10.1007/978-3-030-75452-5
20. Jung, A., Bleistein, T., Reis, M., Cheng, X., Redenbach, C., Diebels, S.: Multiscale microsphere modelling of open-cell metal foams enriched by statistical analysis of geometric parameters. *Mechanics of Materials* **142**, 103295 (2020)
21. Jung, A., Diebels, S.: Microstructural characterisation and experimental determination of a multiaxial yield surface for open-cell aluminium foams. *Materials & Design* **131**, 252–264 (2017)

22. Kabel, M., Andrä, H.: Fast numerical computation of precise bounds of effective elastic moduli. *ITWM Berichte* **224**, 1–16 (2013)
23. Kabel, M., Fink, A., Schneider, M.: The composite voxel technique for inelastic problems. *Comp. Meth. Appl. Mech. Eng.* **322**, 396–418 (2017)
24. Kabel, M., Fliegner, S., Schneider, M.: Mixed boundary conditions for fft-based homogenization at finite strains. *Computational Mechanics* **67**, 193–210 (2016)
25. Kabel, M., Merkert, D., Schneider, M.: Use of composite voxels in FFT-based homogenization. *Comp. Meth. Appl. Mech. Eng.* **294**, 168–188 (2015)
26. Kanit, T., Forest, S., Galliet, I., Mounoury, V., Jeulin, D.: Determination of the size of the representative volume element for random composites: statistical and numerical approach. *International Journal of Solids and Structures* **40**(13), 3647–3679 (2003). DOI [https://doi.org/10.1016/S0020-7683\(03\)00143-4](https://doi.org/10.1016/S0020-7683(03)00143-4)
27. Kendall, D.: Foundations of a theory of random sets. In: *Stochastic Geometry. A Tribute to the Memory of Rollo Davidson*. Wiley (1974)
28. Kröner, E.: Bounds for effective elastic moduli of disordered materials. *Journal of the Mechanics and Physics of Solids* **25**, 127–155 (1977)
29. Lang, C., Ohser, J., Hilfer, R.: On the analysis of spatial binary images. *Journal of Microscopy* **203**, 303–313 (2001)
30. Lautensack, C.: Random Laguerre Tessellations. Ph.D. thesis, Universität Karlsruhe, Verlag Lautensack, Weiler bei Bingen (2007)
31. Lautensack, C.: Fitting three-dimensional Laguerre tessellations to foam structures. *Journal of Applied Statistics* **35**(9), 985–995 (2008)
32. Lautensack, C., Zuyev, S.: Random Laguerre tessellations. *Advances in Applied Probability* **40**(3), 630–650 (2008)
33. Liebscher, A.: Laguerre approximation of random foams. *Philosophical Magazine* **95**(25), 2777–2792 (2015). DOI 10.1080/14786435.2015.1078511. URL <https://doi.org/10.1080/14786435.2015.1078511>
34. Liebscher, A., Redenbach, C.: 3D image analysis and stochastic modelling of open foams. *International Journal of Materials Research* **103**(2), 155 – 161 (2012)
35. Liebscher, A., Redenbach, C.: Statistical analysis of the local strut thickness of open cell foams. *Image Analysis & Stereology* **32**(1), 1–12 (2013). DOI 10.5566/ias.v32.p1-12. URL <https://www.ias-iss.org/ojs/IAS/article/view/944>
36. Lippmann, B., Schwinger, J.: Variational principles for scattering processes. *Physical Review* **79**, 469–480 (1950)
37. Lohmann, G.: *Volumetric Image Analysis*. Wiley-Teubner, Chichester, Leipzig (1998)
38. Luksch J. and Bleistein, T., Koenig, K., Adrien, J., Maire, E., Jung, A.: Microstructural damage behaviour of al foams. *Acta Materialia* **208**, 116739 (2021)
39. Matheron, G.: Ensembles fermés aléatoires, ensembles semi-Markoviens et polyèdres Poissoniens. *Adv. Appl. Probab.* **4**, 508–541 (1972)
40. Matheron, G.: *Random Sets and Integral Geometry*. Wiley, New York (1975)
41. Maurer, C.R., Raghavan, V.: A linear time algorithm for computing exact Euclidean distance transforms of binary images in arbitrary dimensions. *IEEE Trans. Pattern Analysis and Machine Intelligence* **25**(2), 265–270 (2003)
42. Moulinec, H., Suquet, P.: A numerical method for computing the overall response of nonlinear composites with complex microstructure. *Comp. Meth. Appl. Mech. Eng.* **157**, 69–94 (1998)
43. Nagel, W., Ohser, J., Pischang, K.: An integral-geometric approach for the Euler-Poincaré characteristic of spatial images. *J. Microsc.* **198**, 54–62 (2000)
44. Ohser, J., Nagel, W., Schladitz, K.: The Euler number of discretized sets – on the choice of adjacency in homogeneous lattices. In: K.R. Mecke, D. Stoyan (eds.) *Morphology of Condensed Matter, LNP*, vol. 600, pp. 275–298. Springer, Berlin (2002)
45. Ohser, J., Nagel, W., Schladitz, K.: The Euler number of discretised sets – surprising results in three dimensions. *Image Anal. Stereol.* **22**, 11–19 (2003)
46. Ohser, J., Schladitz, K.: *3d Images of Materials Structures – Processing and Analysis*. Wiley VCH, Weinheim (2009)

47. Otsu, N.: A threshold selection method from gray level histograms. *IEEE Trans. Systems, Man and Cybernetics* **9**, 62–66 (1979)
48. Rack, A., Helfen, L., Baumbach, T., Kirste, S., Banhart, J., Schladitz, K., Ohser, J.: Analysis of spatial cross-correlations in multi-constituent volume data. *Journal of Microscopy* **232**(2), 282–292 (2008)
49. Redenbach, C.: Microstructure models for cellular materials. *Computational Materials Science* **44**(4), 1397–1407 (2009)
50. Redenbach, C., Shklyar, I., Andrä, H.: Laguerre tessellations for elastic stiffness simulations of closed foams with strongly varying cell sizes. *International Journal of Engineering Science* **50**(1), 70–78 (2012). DOI <https://doi.org/10.1016/j.ijengsci.2011.09.002>. URL <https://www.sciencedirect.com/science/article/pii/S0020722511001807>
51. Schladitz, K., Ohser, J., Nagel, W.: Measurement of intrinsic volumes of sets observed on lattices. In: A. Kuba, L.G. Nyul, K. Palagyi (eds.) *13th International Conference on Discrete Geometry for Computer Imagery, LNCS*, vol. 4245, pp. 247–258. DGCI, Szeged, Hungary, Springer, Berlin, Heidelberg, New York (2006)
52. Schladitz, K., Peters, S., Reinel-Bitzer, D., Wiegmann, A., Ohser, J.: Design of acoustic trim based on geometric modeling and flow simulation for non-woven. *Computational Materials Science* **38**(1), 56–66 (2006)
53. Schladitz, K., Redenbach, C., Sych, T., Godehardt, M.: Model based estimation of geometric characteristics of open foams. *Methodology and Computing in Applied Probability* **14**, 1011–1032 (2012)
54. Schneider, M.: A review of nonlinear FFT-based computational homogenization method. *Acta Mechanica* **232**, 2051–2100 (2021)
55. Schneider, M., Ospald, F., Kabel, M.: Computational homogenization of elasticity on a staggered grid. *International Journal for Numerical Methods in Engineering* **105**, 693–720 (2016)
56. Schneider, R.: *Convex Bodies. The Brunn–Minkowski Theory*. No. 44 in *Encyclopedia of Mathematics and Its Application*. Cambridge University Press, Cambridge (1993)
57. Schneider, R., Weil, W.: *Stochastic and Integral Geometry. Probability and Its Applications*. Springer, Heidelberg (2008)
58. Serra, J.: *Image Analysis and Mathematical Morphology*, volume 1. Academic Press, London (1982)
59. Spanne, P., Thovert, J.F., Jacquin, C.J., Lindquist, W.B., Jones, K.W., Adler, P.M.: Synchrotron computed microtomography of porous media: Topology and transports. *Phys. Rev. Lett.* **73**, 2001–2004 (1994). DOI [10.1103/PhysRevLett.73.2001](https://doi.org/10.1103/PhysRevLett.73.2001). URL <https://link.aps.org/doi/10.1103/PhysRevLett.73.2001>
60. Spettl, A., Brereton, T., Duan, Q., Werz, T., III, C.E.K., Kroese, D.P., Schmidt, V.: Fitting laguerre tessellation approximations to tomographic image data. *Philosophical Magazine* **96**(2), 166–189 (2016). DOI [10.1080/14786435.2015.1125540](https://doi.org/10.1080/14786435.2015.1125540). URL <https://doi.org/10.1080/14786435.2015.1125540>
61. Staub, S., Andrä, H., Kabel, M.: Fast fft based solver for rate-dependent deformations of composites and nonwovens. *Journal of Solids and Structures* **154**, 33–42 (2018)
62. Suquet, P.: *Elements of homogenization for inelastic solid mechanics. Homogenization Techniques for Composite Materials*, Springer-Verlag, Berlin p. 193–278 (1985)
63. Tek, F.B., Dempster, A.G., Kale, I.: Blood cell segmentation using minimum area watershed and circle Radon transformations. In: C. Ronse, L. Najman, E. Decencière (eds.) *Proc. Int. Symp. on Mathematical Morphology, Computational Imaging and Vision*, vol. 30, pp. 441–454. Springer, Dordrecht (2005)
64. Ulrich, D., Hildebrand, T., Rietbergen, van, B., Müller, R., Rüeegsegger, P.: The quality of trabecular bone evaluated with micro-computed tomography, FEA and mechanical testing. In: G. Lowet, P. Rüeegsegger, H. Weinans (eds.) *Bone research in biomechanics, Studies in health technology and informatics*, pp. 97–112. IOS Press, Netherlands (1997)
65. Vecchio, I., Redenbach, C., Schladitz, K., Kraynik, A.: Improved models of solid foams based on soap froth. *Computational Materials Science* **120**, 60–69 (2016)

66. Vincent, L., Soille, P.: Watersheds in digital spaces: An efficient algorithm based on immersion simulation. *IEEE Transactions on Pattern Analysis and Machine Intelligence* **13**(6), 583–598 (1991)
67. Weaire, D., Hutzler, S.: *The Physics of Foams*. Oxford University Press, Oxford (1999)
68. Zeller, R., Dederichs, P.: Elastic constants of polycrystals. *physica status solidi (b)* **55**, 831–842 (1973)